INTERNATIONAL JOURNAL FOR NUMERICAL METHODS IN FLUIDS
Int. J. Numer. Meth. Fluids 2002; **39**:189–211 (DOI: 10.1002/fld.241)

Finite element analysis of vortex shedding using equal order interpolations

Y. J. Jan*,†

Department of Marine Engineering, National Kao-Hsiung Institute of Marine Technology, Kao-Hsiung(811), Taiwan

SUMMARY

An operator splitting and element-by-element conjugated gradient solver, and equal order interpolations are applied for solving time dependent Navier–Stokes (NS) equations to simulate flow induced vortex shedding in the present study. In addition, the convection term is corrected by balanced tensor diffusivity, which can stabilize the numerical simulation and overcome the numerical oscillations. The evolution of the interested flowing properties with time is analyzed by using spectral analysis. The developed code has been validated by the application of two examples: a driven cavity flow and a flow induced vortex vibration. Results from the first example for Reynolds number $Re = 10^3$ and $Re = 10^4$ are compared with other numerical simulations. Results from the second example, uniform flow past a square rod over a wide range of high Reynolds numbers from $Re = 10^3 \sim 10^5$, are compared with experimental data and other numerical studies. Copyright © 2002 John Wiley & Sons, Ltd.

KEY WORDS: operator splitting; conjugated gradient solver; equal order interpolations; spectral analysis; high Reynolds numbers

1. INTRODUCTION

It is well known that vortex shedding is generated while fluid flow passes the bluff body [1–11]. This phenomenon has drawn much attention particularly in flow separation and the interference between vortices, which is of considerable significance in industry. For example, the flow past a bluff body near a sliding wall has been of interest for several years in the automotive industry, especially to reduce drag for highly fuel-efficient vehicles. Recently, a marked interest in such flows has arisen in relation to magnetic disc-storage devices in the computer-peripherals industry. More recently, a vortex meter [9, 12] has widely been used in industry and its principle is based on a constant Strouhal number for a well established turbulent flow, i.e. a Reynolds number greater than around 10^4. The Strouhal number is given by $St \equiv [(fD)/(U_b)]$, where f is the frequency of vortex shedding, D the width of the bluff body and U_b a characteristic velocity. When St is a constant, this implies that, under this

*Correspondence to: Yih-Jena Jan, P.O. Box 830, Hsin-Chu City 300, Taiwan.
†E-mail: yjjan@mail.nkimt.edu.tw

Received July 2000
Revised August 2001

condition, frequency is proportional to velocity and therefore volume rate, thus providing the basis of a flow meter. In this study, an investigation of the two-dimensional, unsteady flow past a bluff body, a square rod, is made to compare with the research of Arnal *et al.* [2] and experimental data of Okajima [8] because of its similarity to a vortex flow meter.

The finite element method has been extensively used in fluid flow simulation. Benchmark strategies for solving Navier–Stokes (NS) equations can be classified into two categories. One is to solve for $(\underline{\mathbf{U}}, P)$ directly [13] by using the well-known mixed formulation. The advantages of this kind of method are the ease of physical interpretation and the ease with which boundary conditions can be specified. However, the numerical conservation of mass is not accurately satisfied during numerical integration. Therefore, for high Reynolds number flow simulation this would eventually lead to divergence. The other is to use the stream function and vorticity function [14, 15] for predicting the flow field, which automatically satisfies mass balance. Consequently a high Reynolds number flow could usually be predicted easily. However, the boundary conditions of vorticity are difficult to define. Additionally, there is no stream function definition in three-dimensional formulation, although streamlines do exist. With these limitations, it is impossible to extend this formulation to a three-dimensional fluid flow simulation except in the case of axial symmetry. It is also known from the matrix analysis that the order of pressure shape function is less than that of velocity while using the mixed formulation to solve the $(\underline{\mathbf{U}}, P)$ directly [13, 16]. The proposed method here applied to the simulation of vortex shedding is to use $(\underline{\mathbf{U}}, P)$ formulation with equal order interpolations without solving the continuity equation such that this formulation can be easily extended to high Reynolds numbers flow simulation.

To ensure a near optimal mesh, it is noted that grids near the bluff body are needed to be refined. Therefore, unstructured grids are designed to meet this requirement and to avoid using redundant structured grids. In the finite element analysis, Jan *et al.* [16] present a T4/C3 (bubble) element to save computational memory and therefore to accelerate the computation associated with a smaller frontal width. Jan *et al.* [16] used a direct mixed formulation to advance in a stepwise manner. In order to simulate high Reynolds number flows, an operator splitting technique is applied which automatically satisfies the mass conservation equation and thus results in the positive definite Poisson type equation. Because of the positive definite matrix [17], an element-by-element conjugate gradient solver [17, 18] can be implemented into the code to speed up the computation. Additionally, balanced tensor diffusivity (BTD) [19–21] is used to minimize the time integration errors and has the upwinding effect which stabilizes the convection term for high Reynolds number flow simulations. Consequently, the physically present vortex shedding could be predicted without an unrealistic numerically oscillating flow pattern. To implement the code, equal order interpolations, such as three nodes and four nodes shape functions, are adopted in Example 1. Three nodes shape functions are used in Example 2. The computed results show excellent agreement with experiment data [8, 22] as well as other numerical studies [2, 23].

2. FLUID FLOW EQUATIONS

The NS equations governing a two-dimensional incompressible fluid flow can be expressed in a non-dimensional form as

$$\frac{\partial \underline{\mathbf{U}}}{\partial t} + \underline{\mathbf{U}} \bullet \underline{\nabla}\, \underline{\mathbf{U}} = -\underline{\nabla} P + \underline{\mathbf{F}} + \underline{\nabla} \bullet \frac{1}{Re}\, \underline{\nabla}\, \underline{\mathbf{U}} \tag{1}$$

The principle of mass conservation must not be violated, and is represented by

$$\underline{\nabla} \bullet \underline{\mathbf{U}} = 0 \tag{2}$$

In which $\underline{\mathbf{U}}, \underline{\mathbf{F}}$ are the vectors of non-dimensional velocity and body force; P and Re are the pressure and Reynolds number, respectively. The dimensionless variables are defined by

$$x = \frac{\tilde{x}}{D}, \quad y = \frac{\tilde{y}}{D}, \quad t = \frac{\tilde{t}U_b}{D}, \quad \underline{\mathbf{U}} = \frac{\underline{\tilde{\mathbf{U}}}}{U_b}, \quad P = \frac{\tilde{P}}{\rho U_b^2}, \quad Re = \frac{\rho U_b D}{\mu}$$

In which U_b, ρ, μ, D are the characteristic magnitude of velocity, the fluid density, the fluid viscosity, and the characteristic length, respectively. The tilde denotes a dimensional variable. It is noted that the time, $\tilde{t}$, has been normalized with the convective time scale, $T_C = D/U_b$, which is much smaller than the viscous time scale, $T_D = \rho D^2/\mu$, for an oscillatory vortex shedding flow.

An operator splitting and element-by-element conjugated gradient solver, and equal order interpolations are applied for solving time dependent NS equations in the present study. The employed projection technique is first-order accuracy in time [15]. To overcome the numerical oscillation and to stabilize the high Reynolds number flow simulation, a BTD [19–21] is introduced into the discrete NS equations to compensate the time integration error and thus the convection term is corrected. Consequently, vortex shedding can be obtained for fluid flow past a bluff body. The convection term is defined as Equation (3)

$$\underline{\mathbf{f}}_{\text{adv}} = -(\underline{\mathbf{U}} \bullet \underline{\nabla})\underline{\mathbf{U}} \tag{3}$$

The BTD term could be obtained by Equation (4).

$$\underline{\mathbf{B}} \equiv \frac{\Delta t}{2}(\underline{\mathbf{U}} \bullet \underline{\nabla})\underline{\mathbf{f}}_{\text{adv}} \tag{4}$$

Where $\underline{\mathbf{B}}$ represents the BTD vector and Δt is the non-dimensional time step size. The direct mixed formulation of the NS equations with the finite element method results in matrices which are neither symmetric nor positive definite. To meet the positive definite requirement and to accelerate the convergence of fluid flow simulation in every single time step, an operator splitting technique is adopted. Adding Equation (4) into the discrete NS equation, Equation (5) is obtained as follows.

$$\frac{\underline{\mathbf{U}}^{k+1} - \underline{\mathbf{U}}^k}{\Delta t} = \underline{\mathbf{f}}_{\text{adv}}^k - \frac{\Delta t}{2}(\underline{\mathbf{U}}^k \bullet \underline{\nabla})\underline{\mathbf{f}}_{\text{adv}}^k - \underline{\nabla} P^{k+1} + \underline{\mathbf{F}}^k + \underline{\nabla} \bullet \frac{1}{Re}\underline{\nabla}\underline{\mathbf{U}}^k \tag{5}$$

In which k represents the kth time step. The basic idea of operator splitting, which is also called time splitting or the method of fractional steps [24–26] is, in general, a method of approximation of the evolution equations based on decomposition of the operators they originally contain. In this analysis, the operator splitting procedure can be summarized in the following three steps. The first step is to obtain Equation (7) by splitting Equation (6) from Equation (5).

$$\frac{\underline{\mathbf{U}}^* - \underline{\mathbf{U}}^k}{\Delta t} = \underline{\mathbf{f}}_{\text{adv}}^k - \frac{\Delta t}{2}(\underline{\mathbf{U}}^k \bullet \underline{\nabla})\underline{\mathbf{f}}_{\text{adv}}^k + \underline{\mathbf{F}}^k + \underline{\nabla} \bullet \frac{1}{Re}\underline{\nabla}\underline{\mathbf{U}}^k \tag{6}$$

$$\underline{\mathbf{U}}^{k+1} = \underline{\mathbf{U}}^* - \Delta t(\underline{\nabla} P^{k+1}) \tag{7}$$

A fictitious or provisional velocity $\underline{\mathbf{U}}^*$ can be solved from Equation (6) explicitly. Secondly, Equation (8) for the pressure P^{k+1} is derived by making the divergence of Equation (7) and by enforcing the principle of mass conservation ($\underline{\boldsymbol{\nabla}} \bullet \underline{\mathbf{U}}^{k+1} = 0$). At the final step, $\underline{\mathbf{U}}^{k+1}$ is calculated from Equation (7) by the solved pressure, P^{k+1}.

$$\underline{\boldsymbol{\nabla}}^2 P^{k+1} = \frac{1}{\Delta t} \underline{\boldsymbol{\nabla}} \bullet \underline{\mathbf{U}}^* \tag{8}$$

To start the solution procedure, proper boundary conditions are required for these equations of motion. Fortunately, the essential feature of the fractional step or operator splitting method is that the numerical solution is independent of the value $\underline{\mathbf{U}}^*$ on the boundary (Γ) and more precisely of $\underline{\mathbf{U}}^* \bullet \underline{\mathbf{n}}|_\Gamma$. In the present study, $\underline{\mathbf{U}}^*|_\Gamma = \underline{\mathbf{U}}^{k+1}|_\Gamma$ is selected for convenience and this selection is purely numerical [15, 24, 25]. A non-slip boundary condition is proposed for the solid boundary and a traction free boundary condition is adopted for solving Equation (8) at a specified outlet. The traction free boundary condition [4, 16] is described by

$$P - \underline{\mathbf{n}} \bullet \underline{\underline{\boldsymbol{\tau}}} \bullet \underline{\mathbf{n}} = 0 \tag{9}$$

Where the stress tensor is defined as $\underline{\underline{\boldsymbol{\tau}}} = \frac{1}{Re}(\underline{\nabla}\,\underline{\mathbf{U}} + (\underline{\boldsymbol{\nabla}}\,\underline{\mathbf{U}})^{\mathrm{tr}})$ and $\underline{\mathbf{n}}$ is an outward normal unit vector. For unsteady flow simulations, the entire procedure is repeated for each time step.

3. COMPUTATIONAL METHOD

Applying the Galerkin finite element method to Equations (6)–(8) and dropping all boundary-conditions-generated surface integrals, the resulting Equations (10)–(14) are expressed as

$$\sum_1^{m^e} M_{ab}^e u_b^* = \sum_1^{m^e} M_{ab}^e u_b^k - \Delta t \sum_1^{m^e} \left(C_{ab}^e + B_{ab}^e + \frac{1}{Re} D_{ab}^e \right) u_b^k \tag{10}$$

$$\sum_1^{m^e} M_{ab}^e v_b^* = \sum_1^{m^e} M_{ab}^e v_b^k - \Delta t \sum_1^{m^e} \left(C_{ab}^e + B_{ab}^e + \frac{1}{Re} D_{ab}^e \right) v_b^k \tag{11}$$

$$\sum_1^{m^e} D_{ab}^e P_b^{k+1} = -\frac{1}{\Delta t} \sum_1^{m^e} (D_{x,ab}^e u_b^* + D_{y,ab}^e v_b^*) \tag{12}$$

$$\sum_1^{m^e} M_{ab}^e u_b^{k+1} = \sum_1^{m^e} M_{ab}^e u_b^* - \Delta t \sum_1^{m^e} D_{x,ab}^e P_b^{k+1} \tag{13}$$

$$\sum_1^{m^e} M_{ab}^e v_b^{k+1} = \sum_1^{m^e} M_{ab}^e v_b^* - \Delta t \sum_1^{m^e} D_{y,ab}^e P_b^{k+1} \tag{14}$$

Where the element matrices associated with Equations (10)–(14) are evaluated on each element as

$$M_{ab}^e \equiv \int_{\Lambda^e} N_a N_b \, \mathrm{d}\Lambda^e \tag{15}$$

$$C^e_{ab} \equiv \int_{\Lambda^e} N_a(\underline{\mathbf{U}}^k \cdot \underline{\nabla} N_b)\,\mathrm{d}\Lambda^e \tag{16}$$

$$B^e_{ab} \equiv \frac{\Delta t}{2} \int_{\Lambda^e} (\underline{\mathbf{U}}^k \cdot \underline{\nabla} N_a)(\underline{\mathbf{U}}^k \cdot \underline{\nabla} N_b)\,\mathrm{d}\Lambda^e \tag{17}$$

$$D^e_{ab} \equiv \int_{\Lambda^e} \underline{\nabla} N_a \cdot \underline{\nabla} N_b\,\mathrm{d}\Lambda^e \tag{18}$$

$$D^e_{x,ab} \equiv \int_{\Lambda^e} N_a \frac{\partial N_b}{\partial x}\,\mathrm{d}\Lambda^e \tag{19}$$

$$D^e_{y,ab} \equiv \int_{\Lambda^e} N_a \frac{\partial N_b}{\partial y}\,\mathrm{d}\Lambda^e \tag{20}$$

In which N_a N_b are the shape functions defined by the linear triangle element shape function or the quadrilateral element function in this study, u_b and v_b the velocity at the nodal points in x- and y-direction respectively. Those element matrices defined by Equation (15)–(20) are given in Appendix A. In addition, Equation (12) can be solved by conjugate gradient method (CG [17, 18]). In exact arithmetic, the conjugate gradient method is guaranteed to converge within m iterations, where m is the order of the matrix (in this study, m is the number of unknown pressure at the nodal points). In practice, the number of iterations is strongly dependent upon the condition number of the matrix. This is more of theoretical interest than a practically usable criterion. In this study, the convergence criterion is that the least of the normalized residuals for pressure summed over all the control volumes (elements) in the nodal point should be less than a prescribed value, usually 10^{-5}. For the calculations, the time step size Δt is selected by Equation (21) derived by a simplified analysis for a one-dimensional case [4] and it is clear that Δt becomes smaller as decreasing characteristic mesh size δ.

$$\Delta t < \frac{\delta^2}{2/Re + \delta} \tag{21}$$

4. NUMERICAL RESULTS

The hydraulic force is important in many physical and engineering problems encountered in fluid dynamics. By definition, the force $\tilde{\underline{\mathbf{F}}}_S$ acting on the bluff body can be expressed by

$$\begin{aligned}\tilde{\underline{\mathbf{F}}}_S &= \left(\oint_\Gamma (P\underline{\mathbf{n}}_s - \frac{1}{Re}(\underline{\nabla}\,\underline{\mathbf{U}} + (\underline{\nabla}\,\underline{\mathbf{U}})^{\mathrm{tr}}) \bullet \underline{\mathbf{n}}_s)\,\mathrm{d}\Gamma \right)(\rho U_b^2 D) \\ &= \tilde{F}_D \underline{\mathbf{i}} + \tilde{F}_L \underline{\mathbf{j}}\end{aligned} \tag{22}$$

$$\tilde{F}_D = \left(\frac{1}{2}\rho U_b^2 D\right) C_D \tag{23}$$

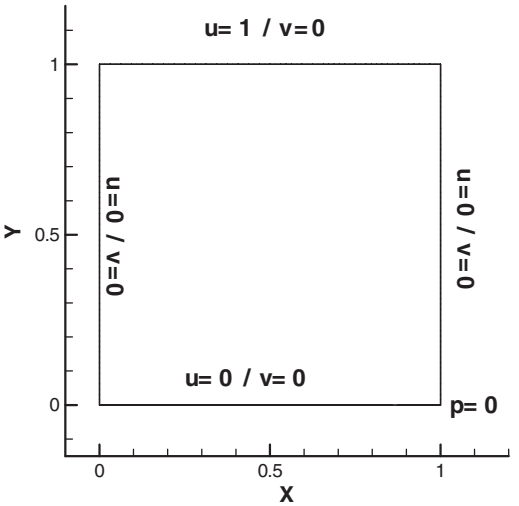

Figure 1. Geometric layout of driven cavity flow.

$$\tilde{F}_L = \left(\frac{1}{2}\rho U_b^2 D\right) C_L \tag{24}$$

$$C_D = 2\oint_\Gamma \left(\left(P - 2\frac{1}{Re}\frac{\partial u}{\partial x}\right)\mathrm{d}y + \frac{1}{Re}\left(\frac{\partial u}{\partial y} + \frac{\partial v}{\partial x}\right)\mathrm{d}x\right) \tag{25}$$

$$C_L = -2\left(\oint_\Gamma \left(\left(P - 2\frac{1}{Re}\frac{\partial v}{\partial y}\right)\mathrm{d}x + \frac{1}{Re}\left(\frac{\partial u}{\partial y} + \frac{\partial v}{\partial x}\right)\mathrm{d}y\right)\right) \tag{26}$$

In which C_D represents the drag coefficient, C_L the lift or vibration coefficient, $\tilde{F}_D$ the drag force, $\tilde{F}_L$ the lift force and Γ the boundary (clockwise) of bluff body. Here u and v stand for the velocity in x- and y-direction, respectively. The notations $\underline{\mathbf{i}}$ and $\underline{\mathbf{j}}$ are the unit base vectors of the Cartesian coordinate in x- and y-direction, respectively. It should be mentioned that $\underline{\mathbf{n}}_s$ is the unit normal vector (directed into the bluff body) when the integration is carried out.

The flow property C_D (or C_L) varies with Re and St number. The St, defined as $St = fD/U_b$ where f is the frequency of vortex shedding, is obtainable from the flow property C_D or C_L. In other words, C_D or C_L can be recorded for every single time step for a given Reynolds number and consequently the Strouhal number is obtained from the spectral analysis [17].

Example 1: Wall-driven cavity flow

The driven cavity flow is well known as a standard test problem in fluid flow simulations. In this analysis, two different Reynolds numbers, $Re = 10^3$ and $Re = 10^4$, are tested. The problem of interest is sketched in Figure 1 including the geometric configuration and boundary conditions. The triangle mesh layout, which contains 6866 elements and 3562 nodal points, is

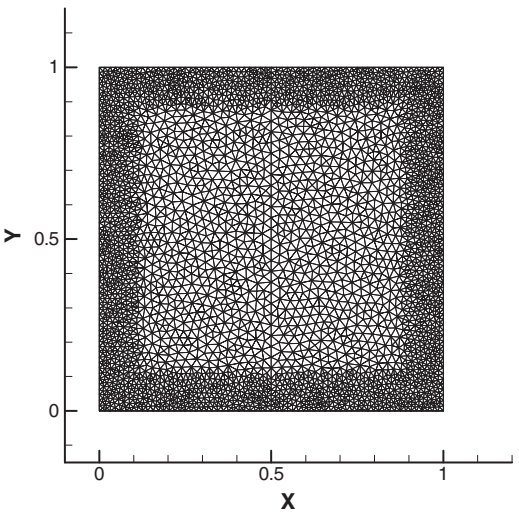

Figure 2. Mesh layout of driven cavity flow (6866 elements, 3562 nodes).

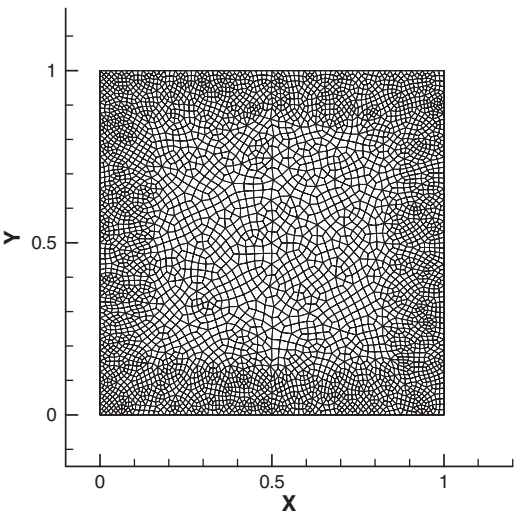

Figure 3. Mesh layout of driven cavity flow (4400 elements, 4529 nodes).

shown in Figure 2, and the quadrilateral mesh, which contains 4400 elements and 4529 nodal points, is shown in Figure 3. To study the effect of mesh size, medium-sized mesh (5716 elements and 5305 nodes) for a quadrilateral element is also shown in Figure 4 and fine mesh (8874 elements and 9131 nodes) is shown in Figure 5. The simple relation between Δt and the characteristic mesh size δ, which is roughly approximated by the square root of the minimum area of elements, is given by Equation (21). The finest area of the triangle elements shown

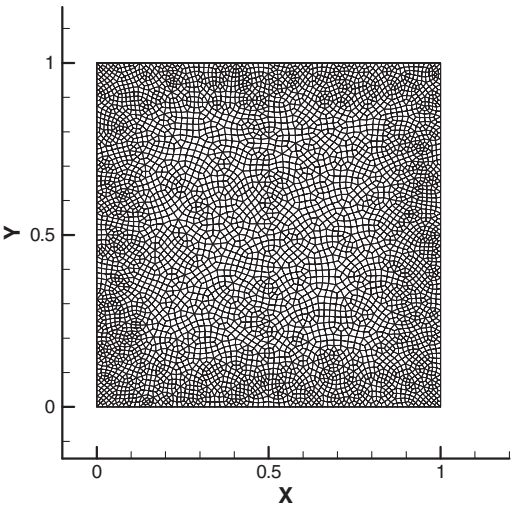

Figure 4. Mesh layout of driven cavity flow (5716 elements, 5305 nodes).

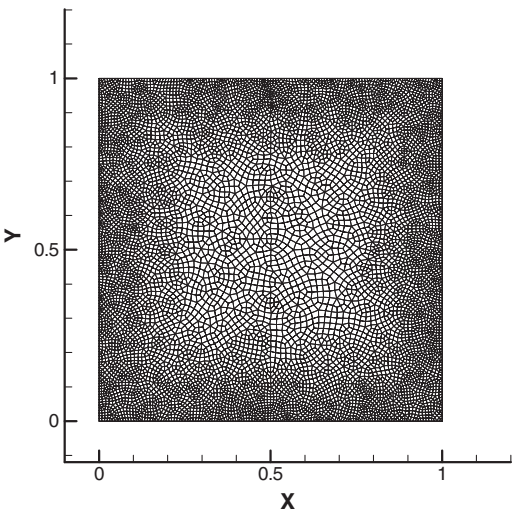

Figure 5. Mesh layout of driven cavity flow (8874 elements, 9131 nodes).

in Figure 2 is 0.000037 and therefore δ is approximated by 0.006. Conservatively, $\Delta t = 0.005$ and $\Delta t = 0.003$ are selected in this study. The choice of Δt for quadrilateral mesh is also carried out in a similar way. A moving wall with a velocity $u = 1.0$ moves from left to right. The fluid inside the cavity is initially motionless. As shown in Figures 6 and 7, the evolution of iteration number with time shows the solution is converged within m iterations at each time step in which m is the number of the unknown pressures in Equation (12). All the calculations were performed on a Pentium III 450, and the program was written in

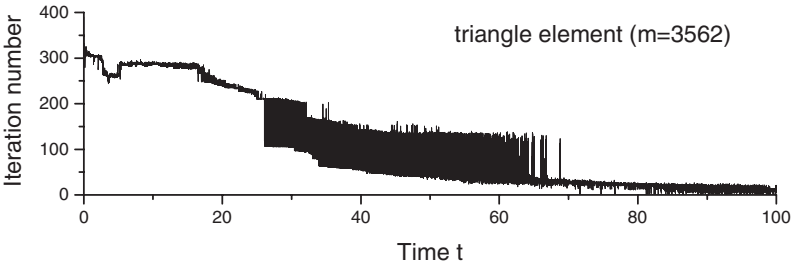

Figure 6. Evolution of iteration number with time ($\Delta t = 0.005,\ Re = 10^3$) (6866 triangle elements, 3562 nodes).

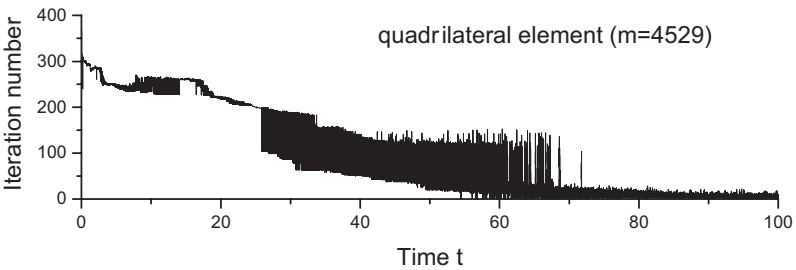

Figure 7. Evolution of iteration number with time ($\Delta t = 0.005,\ Re = 10^3$) (4400 quadrilateral elements, 4529 nodes).

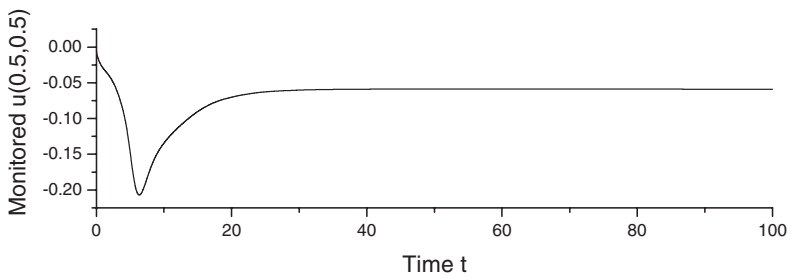

Figure 8. Convergence history of monitored $u(0.5, 0.5)$ ($\Delta t = 0.005,\ Re = 10^3$) (6866 triangle elements, 3562 nodes).

Fortran language using Lahey–Fortran 90-V4.5 compiler. The computing time for completing 20 000 time steps is about 490 min for the triangle element and 140 min for the quadrilateral element at $Re = 10^3$. Therefore, the computational time ratio between the two test cases is $[(490)/(140)] = 3.5$, which is attributed to the condition numbers, the type of elements and the number of elements. To obtain the steady state solution of driven cavity flow, the evolution of the horizontal velocity u with time at the point (0.5, 0.5) is plotted in Figures 8 and 9 for $Re = 10^3$ and in Figures 10 and 11 for $Re = 10^4$. The streamline contours of the fully

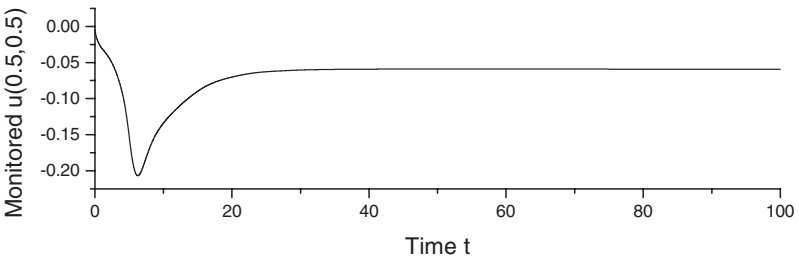

Figure 9. Convergence history of monitored $u(0.5, 0.5)$ ($\Delta t = 0.005$, $Re = 10^3$) (4400 quadrilateral element, 4529 nodes).

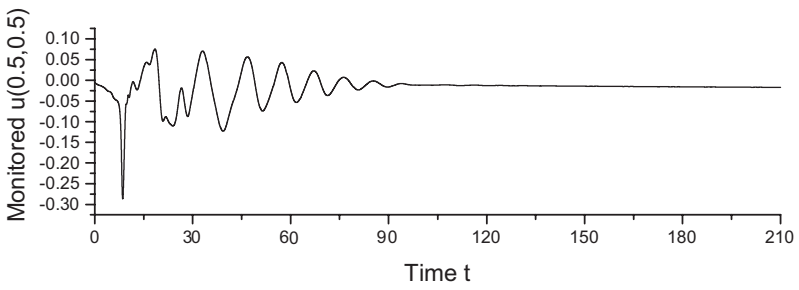

Figure 10. Convergence history of monitored $u(0.5, 0.5)$ ($\Delta t = 0.003$, $Re = 10^4$) (6866 triangle elements, 3562 nodes).

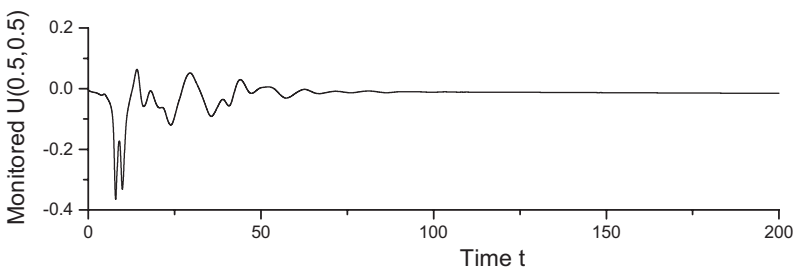

Figure 11. Convergence history of monitored $u(0.5, 0.5)$ ($\Delta t = 0.005$, $Re = 10^4$) (4400 quadrilateral elements, 4529 nodes).

developed steady flow are shown in Figures 12 and 13 for $Re = 10^3$ and in Figures 14 and 15 for $Re = 10^4$. A magnified view of a secondary vortex at the right-hand lower corner is illustrated in Figure 16. The corresponding locations of various vortices, which are in excellent agreement with numerical results of Ghia *et al.* [23], are listed in Table I. Additionally, the numerical results of velocity profiles u along the vertical central line are in very good agreement with data from Reference [23] as presented in Figures 17 and 18 for $Re = 10^3$. It is noted that the numerical results for different time increments also agree very well with

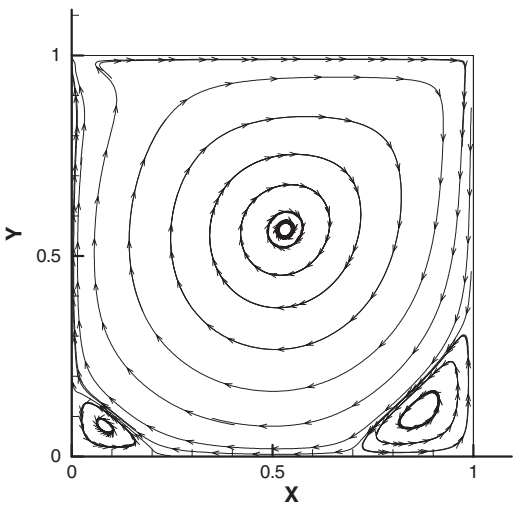

Figure 12. Streamlines of driven cavity flow ($\Delta t = 0.003,\ t = 60,\ Re = 10^3$) (6866 triangle elements, 3562 nodes).

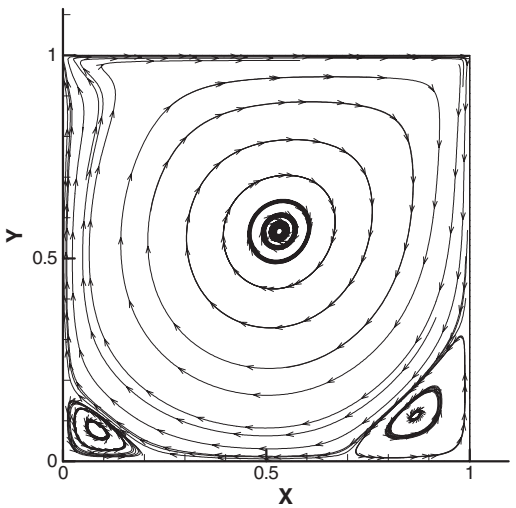

Figure 13. Streamlines of driven cavity flow ($\Delta t = 0.005,\ t = 50,\ Re = 10^3$) (4400 quadrilateral elements, 4529 nodes).

the results from Reference [23]. However, the results for $Re = 10^4$ are different for different time step sizes as shown in Figures 19 and 20. It is evident that the solution is much closer to the numerical results of Reference [23] when the smaller time step $\Delta t = 0.003$ is adopted for the same mesh. This is caused by less upwind effect from BTD through a smaller time step size at high Reynolds number flow. It implies that the spatial resolution on this order of

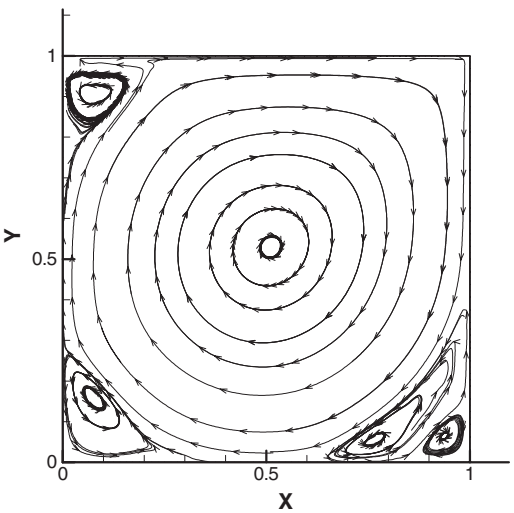

Figure 14. Streamlines of driven cavity flow ($\Delta t = 0.003,\ t = 180,\ Re = 10^4$) (6866 triangle elements, 3562 nodes).

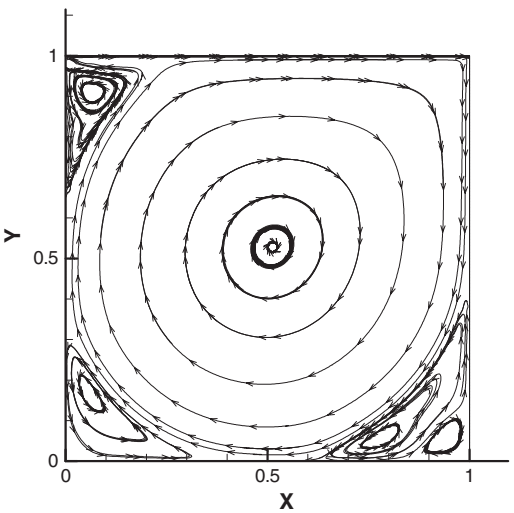

Figure 15. Streamlines of driven cavity flow ($\Delta t = 0.005,\ t = 200,\ Re = 10^4$) (4400 quadrilateral elements, 4529 nodes).

magnitude of mesh size (6866 elements, 3562 nodes) with a proper time step is sufficiently accurate for the purpose of this study and a further test is carried out and is illustrated in Figure 20. Again, the solution obtained by using 4400 quadrilateral elements, 4529 nodes and $\Delta t = 0.01$ is under-predicted as compared with results of Reference [23] due to upwind effect. However this phenomenon can be improved by temporal refinement as shown in Figure 20.

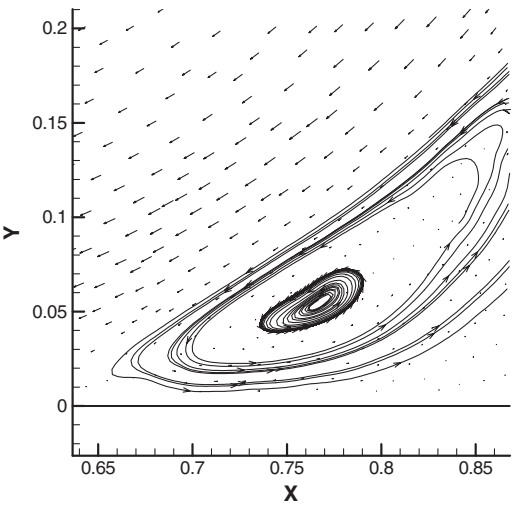

Figure 16. The location of right corner vortex for $Re = 10^4$ (4400 quadrilateral elements, 4529 nodes, $\Delta t = 0.005$, $t = 200$).

Table I. Comparison between Ghia *et al.* [23] and the present study.

Location of vortex	Ghia *et al.* (numerical results)		Present study Triangle element 6866 elements, 3562 nodes, $\Delta t = 0.003$		Present study Quadrilateral element 4400 elements, 4529 nodes, $\Delta t = 0.005$	
	Primary vortex	Right corner vortex	Primary vortex	Right corner vortex	Primary vortex	Right corner vortex
$Re = 10^3$	0.531, 0.563	0.859, 0.109	0.531, 0.565	0.867, 0.113	0.530, 0.563	0.867, 0.115
$Re = 10^4$	0.512, 0.533	0.766, 0.059	0.511, 0.533	0.766, 0.055	0.511, 0.532	0.766, 0.056

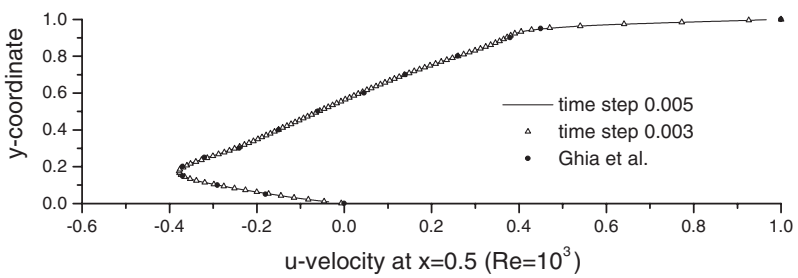

Figure 17. u-velocity on the vertical center line in steady state ($t = 60$, $Re = 10^3$) (6866 triangle elements, 3562 nodes).

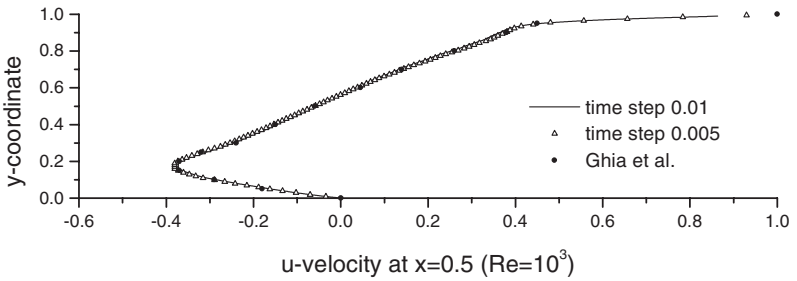

Figure 18. u-velocity on the vertical center line in steady state ($t = 50,\ Re = 10^3$) (4400 quadrilateral elements, 4529 nodes).

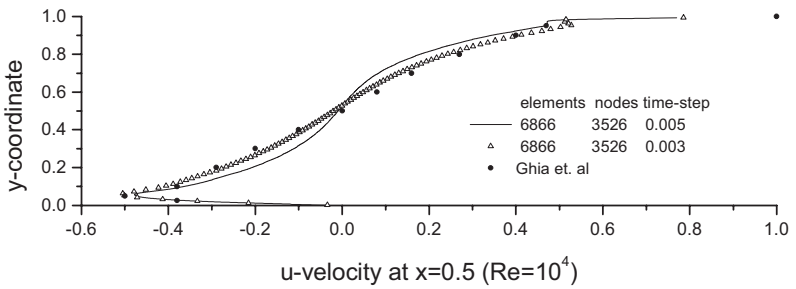

Figure 19. u-velocity on the vertical center line in steady state ($t = 180,\ Re = 10^4$) (6866 triangle elements, 3562 nodes).

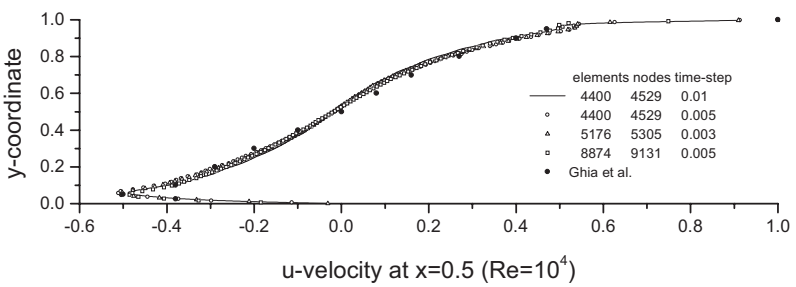

Figure 20. u-velocity on the vertical center line in steady state ($t = 180,\ Re = 10^4$) (quadrilateral element).

The numerical predictions from medium-sized mesh (Figure 4) and the finest mesh (Figure 5) for the time increments around $0.005 \sim 0.003$ do not have as much difference as presented in Figure 20.

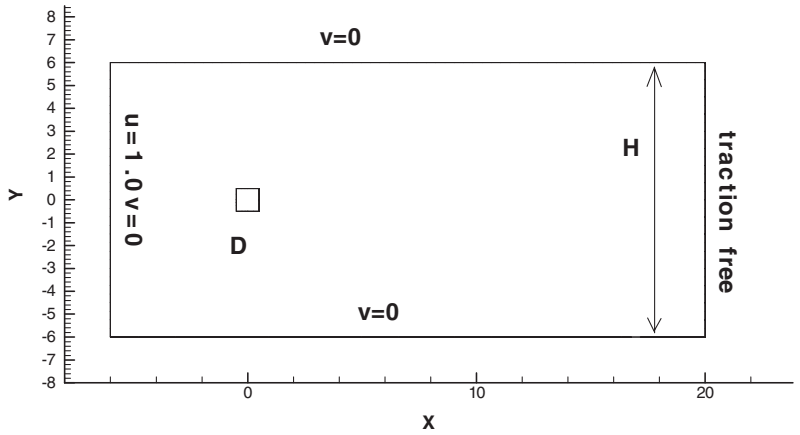

Figure 21. Geometric layout for flow passing a square rod.

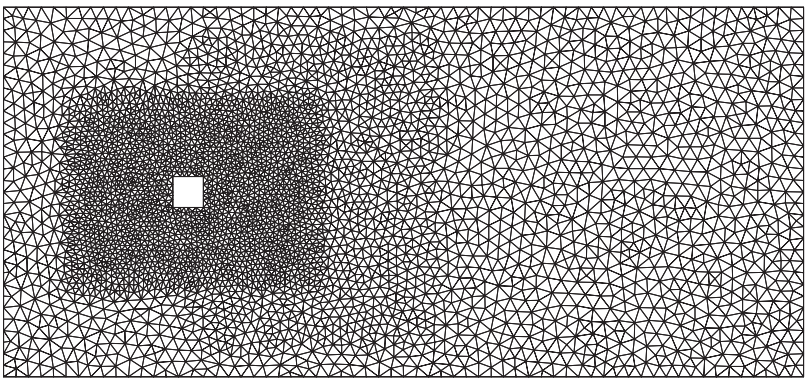

Figure 22. Mesh layout for flow passing square rod (8032 elements, 4122 nodes).

Example 2: Flow induced vibration flow – vortex shedding

The problem of vortex shedding generated while fluid flow passes a bluff body is of importance to validate the numerical code developed in this study. Figure 21 illustrates that a uniform flow at a velocity $u = 1.0$ flows from left to right toward a square rod with characteristic length $D = 1.0$. The non-slip boundary conditions are specified on the surface of the solid square rod and the traction-free boundary conditions are imposed at the downstream in this simulation. The fluid is assumed to be initially motionless.

The finite element mesh of the flow region containing 8032 elements and 4122 nodal points is presented in Figure 22. Since the velocity gradient near the square rod is very steep, finer mesh is needed around this bluff body. The computer simulation started from $t = 0$ to $t = 400$ with a dimensionless time increment, $\Delta t = 0.04$. Streamline contour for $Re = 10^3$ at time instant $t = 275$ is shown in Figure 23, which demonstrates the vibrating velocity. The variation of C_D and C_L, shows evidence of cycle-to-cycle pattern as depicted in Figure 24. The

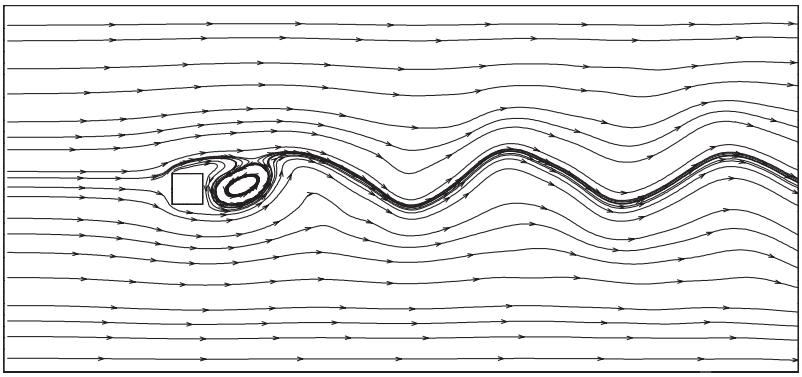

Figure 23. Streamlines for flow passing square rod (8032 elements, 4122 nodes, $\Delta t = 0.04,\ t = 275,\ Re = 10^3$).

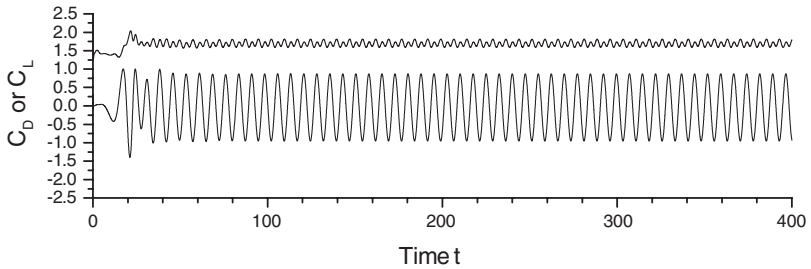

Figure 24. Time history of drag or lift coefficient (8032 elements, 4122 nodes, $\Delta t = 0.04,\ Re = 10^3$).

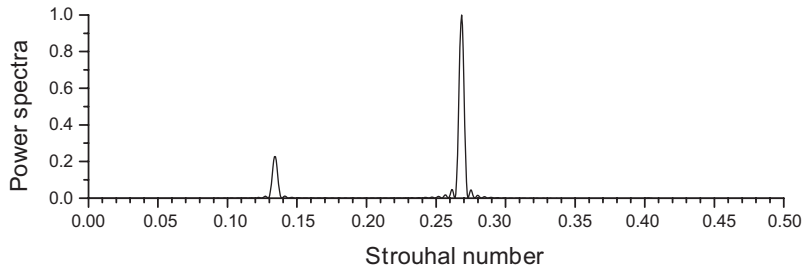

Figure 25. C_D spectral corresponding to $Re = 10^3$ (8032 elements, 4122 nodes, $\Delta t = 0.04$).

fundamental shedding frequency can be obtained by measuring the frequency of the lift oscillation. It is apparent from Figures 25 and 26 that the drag coefficient oscillates twice the frequency of the lift coefficient, which has been reported by Arnal *et al.* [2]. For $Re = 100 \sim 400$, the comparisons of the Strouhal number of the present study with published results [8, 10] are given in Table II. It is clear that the current simulations give less discrepancy as compared

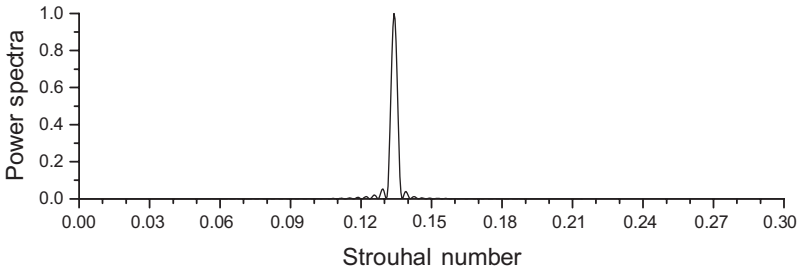

Figure 26. C_L spectral corresponding to $Re = 10^3$ (8032 elements, 4122 nodes, $\Delta t = 0.04$).

Table II. Comparison of Strouhal number of the present study with other published results.

	Strouhal number			
Re	Davis *et al.* [28] (numerical results)	Present study $\Delta t = 0.04$	Present study $\Delta t = 0.01$	Okajima [8] (experiments)
100	0.154	0.139	0.144	$0.135 \sim 0.140$
200		0.148	0.152	$0.140 \sim 0.148$
250	0.165	0.148	0.151	$0.140 \sim 0.148$
300		0.147	0.149	$0.139 \sim 0.140$
400	0.159	0.144	0.138	$0.130 \sim 0.135$

Table III. Spatial and temporal refinement study for $Re = 10^3$.

Mesh	δ	Δt	C_D	St	Arnal *et al.* [2] (numerical results)	Okajima [8] (experiments)	Davis *et al.* [10, 28] (numerical results)
5106 nodes	0.0303	0.02	0.23	0.138	$C_D = 0.22$	$St = 0.125 \sim 0.13$	$C_D = 0.204$
9966 elements		0.03	0.22	0.138	$St = 0.142$		$St = 0.142$
4122 nodes	0.0589	0.01	0.176	0.135			
8032 elements		0.04	0.167	0.134			

with the experimental results [8] while the results of Reference [10] over-predicted. Table III provides a summary of the spatial and temporal refinement comparisons for $Re = 10^3$ and it is clear that the simulated results give over-predictions compared with the experimental data from Okajima [8]. The Strouhal numbers in Figures 26 and 27 (different mesh size) are less than 1 per cent discrepancy. A further test of two different time increments, namely, $\Delta t = 0.01$ and $\Delta t = 0.04$, has been conducted over the Reynolds number range of $Re = 10^3 \sim 10^5$ with the spatial condition of 8032 elements, 4122 nodal points, as plotted in Figure 28. It is clear that the time step $\Delta t = 0.01$ gives the Strouhal number over-predictions in the range of $0.132 \sim 0.150$ compared to the experimental data of Reference [8] and the time step $\Delta t = 0.04$ gives values around $0.127 \sim 0.140$ closer to the experimental data of Reference [8]. The over-predictions compared with data of Reference [8] are probably due to the high

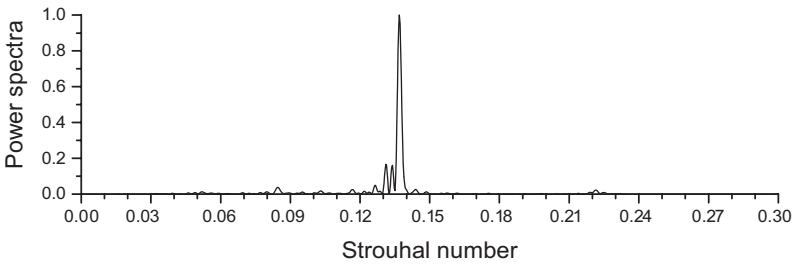

Figure 27. C_L spectral corresponding to $Re = 10^3$ (9966 elements, 5106 nodes, $\Delta t = 0.03$).

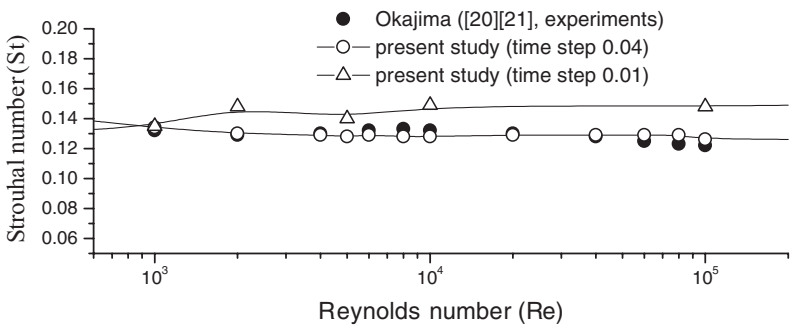

Figure 28. Comparison between experimental results [8, 22] and the present study.

turbulent intensity (0.5 per cent in Okajima [8]) at the inlet; turbulent intensity, however, is completely absent in the numerical simulation. Furthermore, experiments [27] show that the Strouhal number decreases with increasing turbulent level at the inlet. In addition, the effect of the geometric factor, $(D)/(H)$, is introduced in the present study. Davis *et al.* [28] have shown that both the drag coefficient and Strouhal number increase with the ratio of $(D)/(H)$. Numerical over-predictions are also reported by other studies [5, 10, 28]. However, predicted Strouhal numbers using $\Delta t = 0.04$ agree favorably with the experiments as clearly presented in Figure 28. In Figure 28, the Strouhal number is approximated to a constant value for Reynolds number raised to a certain range. The present numerical value (0.127) deviates about 5.8 per cent from the experimental data (0.12) for $Re = \mathrm{O}(10^5)$ [11]. In summary, the computed Strouhal numbers compare reasonably well with experiments [8]. With the nearly constant Strouhal number, frequency is proportional to the bulk velocity U_b (or the volume rate), thus providing the basis of a flow induced vortex meter [7, 12].

5. CONCLUSION

For the transient flow simulation, operator splitting can lead to a positive definite matrix. Consequently, the element-by-element conjugated gradient method of acceleration technique for solving system equations can be implemented into the code and guarantee to obtain the

converged flow field within certain limited iterations. The BTD gives the effect of alleviating the numerical oscillation and therefore stabilizes the high Reynolds number flow simulation. The code successfully implemented on the use of equal order interpolations for velocity and pressure is verified by the application of a driven cavity flow and a flow induced vortex shedding.

ACKNOWLEDGEMENTS

The author would like to express his sincere thanks to the National Science Council of Taiwan for its support under contract NSC89-2611-E-022-006. In addition, the suggestions and comments from reviewer(s) are appreciated.

APPENDIX A: ELEMENT MATRIX

QUADRILATERAL ELEMENT	
ITEM	$(\xi_1,\eta_1)=(-1,-1),\ (\xi_2,\eta_2)=(1,-1),\ (\xi_3,\eta_3)=(1,1),\ (\xi_4,\eta_4)=(-1,1)$
	$\underline{\mathbf{A}}^{\xi}=[A_{11},A_{21}],\ \underline{\mathbf{A}}^{\eta}=[A_{12},A_{22}],\ A_{11}=\frac{1}{4}(y_3+y_4-y_1-y_2),$
	$A_{12}=\frac{1}{4}(y_1+y_4-y_2-y_3)$
	$A_{21}=\frac{1}{4}(x_1+x_2-x_3-x_4),\ A_{22}=\frac{1}{4}(x_2+x_3-x_1-x_4)$
	$\langle\underline{\mathbf{U}}\rangle_e=\frac{\underline{\mathbf{U}}_1+\underline{\mathbf{U}}_2+\underline{\mathbf{U}}_3+\underline{\mathbf{U}}_4}{4},\ S_e=4(A_{11}A_{22}-A_{12}A_{21})$
N_1	$\frac{1}{4}(1-\xi)(1-\eta)$
N_2	$\frac{1}{4}(1+\xi)(1-\eta)$
N_3	$\frac{1}{4}(1+\xi)(1+\eta)$
N_4	$\frac{1}{4}(1-\xi)(1+\eta)$
M^e_{ab}	$\int_{\Lambda^e} N_aN_b\,\mathrm{d}\Lambda^e\approx\frac{1}{4}S_e\delta_{ab},\ \delta_{ab}=\begin{cases}1, & a=b\\ 0, & a\neq b\end{cases}$
$D^e_{x,ab}$	$\int_{\Lambda^e} N_a\frac{\partial N_b}{\partial x}\,\mathrm{d}\Lambda^e=\frac{1}{4}\left(A_{11}\left(1+\frac{1}{3}\eta_a\eta_b\right)\xi_b+A_{12}\left(1+\frac{1}{3}\xi_a\xi_b\right)\eta_b\right)$
$D^e_{y,ab}$	$\int_{\Lambda^e} N_a\frac{\partial N_b}{\partial y}\,\mathrm{d}\Lambda^e=\frac{1}{4}\left(A_{21}\left(1+\frac{1}{3}\eta_a\eta_b\right)\xi_b+A_{22}\left(1+\frac{1}{3}\xi_a\xi_b\right)\eta_b\right)$

D^e_{ab}

$$\int_{\Lambda^e} \underline{\nabla} N_a \cdot \underline{\nabla} N_b \, \mathrm{d}\Lambda^e = \frac{(A_{11})^2 + (A_{21})^2}{S_e} (\xi_a \xi_b) \left(1 + \frac{1}{3} \eta_a \eta_b\right) + \frac{(A_{12})^2 + (A_{22})^2}{S_e} (\eta_a \eta_b) \left(1 + \frac{1}{3} \xi_a \xi_b\right) + \frac{A_{11} A_{12} + A_{21} A_{22}}{S_e} (\xi_a \eta_b + \eta_a \xi_b)$$

C^e_{ab}

$$\int_{\Lambda^e} N_a \underline{\mathbf{U}} \cdot \underline{\nabla} N_b \, \mathrm{d}\Lambda^e = \frac{1}{4} \xi_b \left(1 + \frac{1}{3} \eta_a \eta_b\right) (\langle \underline{\mathbf{U}} \rangle_e \cdot \underline{\mathbf{A}}^{\xi}) + \frac{1}{4} \eta_b \left(1 + \frac{1}{3} \xi_a \xi_b\right) (\langle \underline{\mathbf{U}} \rangle_e \cdot \underline{\mathbf{A}}^{\eta})$$

B^e_{ab}

$$\frac{\Delta t}{2} \int_{\Lambda^e} (\underline{\mathbf{U}} \cdot \underline{\nabla} N_a)(\underline{\mathbf{U}} \cdot \underline{\nabla} N_b) \, \mathrm{d}\Lambda^e = \frac{\Delta t}{2 S_e} ((\langle \underline{\mathbf{U}} \rangle_e \cdot \underline{\mathbf{A}}^{\xi})(\langle \underline{\mathbf{U}} \rangle_e \cdot \underline{\mathbf{A}}^{\xi})(\xi_a \xi_b) \left(1 + \frac{1}{3} \eta_a \eta_b\right) + (\langle \underline{\mathbf{U}} \rangle_e \cdot \underline{\mathbf{A}}^{\eta})(\langle \underline{\mathbf{U}} \rangle_e \cdot \underline{\mathbf{A}}^{\eta})(\eta_a \eta_b) \left(1 + \frac{1}{3} \xi_a \xi_b\right) + (\langle \underline{\mathbf{U}} \rangle_e \cdot \underline{\mathbf{A}}^{\xi})(\langle \underline{\mathbf{U}} \rangle_e \cdot \underline{\mathbf{A}}^{\eta})(\xi_a \eta_b + \eta_a \xi_b))$$

TRIANGLE ELEMENT

ITEM $(\xi_1, \eta_1) = (0,0),\ (\xi_2, \eta_2) = (1,0),\ (\xi_3, \eta_3) = (0,1), A_{11} = y_3 - y_1,\ A_{12} = y_1 - y_2,$

$$A_{21} = x_1 - x_3,$$

$$A_{22} = x_2 - x_1, \langle \underline{\mathbf{U}} \rangle_e = \frac{\underline{\mathbf{U}}_1 + \underline{\mathbf{U}}_2 + \underline{\mathbf{U}}_3}{3}, S_e = \frac{1}{2} (A_{11} A_{22} - A_{12} A_{21}),\ \underline{\mathbf{A}}^{\xi} = [A_{11}, A_{21}],$$

$$\underline{\mathbf{A}}^{\eta} = [A_{12}, A_{22}]$$

N_1 $1 - \xi - \eta$

N_2 ξ

N_3 η

M^e_{ab} $$\int_{\Lambda^e} N_a N_b \, \mathrm{d}\Lambda^e \approx \frac{1}{3} S_e \delta_{ab}, \delta_{ab} = \begin{cases} 1, & a = b \\ 0, & a \neq b \end{cases}$$

$D^e_{x,ab}$ $$\int_{\Lambda^e} N_a \frac{\partial N_b}{\partial x} \, \mathrm{d}\Lambda^e = \frac{1}{6} (A_{11} \xi_b + A_{12} \eta_b)$$

$D^e_{y,ab}$ $$\int_{\Lambda^e} N_a \frac{\partial N_b}{\partial y} \, \mathrm{d}\Lambda^e = \frac{1}{6} (A_{21} \xi_b + A_{22} \eta_b)$$

$$D^e_{ab} \qquad \int_{\Lambda^e} \underline{\nabla} N_a \cdot \underline{\nabla} N_b \, \mathrm{d}\Lambda^e = \frac{(A_{11})^2 + (A_{21})^2}{4S_e} (\xi_a \xi_b) + \frac{(A_{12})^2 + (A_{22})^2}{4S_e} (\eta_a \eta_b) + \frac{A_{11}A_{12} + A_{21}A_{22}}{4S_e} (\xi_a \eta_b + \eta_a \xi_b)$$

$$C^e_{ab} \qquad \int_{\Lambda^e} N_a \underline{\mathbf{U}} \cdot \underline{\nabla} N_b \, \mathrm{d}\Lambda^e = \frac{1}{6} (\langle \underline{\mathbf{U}} \rangle_e \cdot \underline{\mathbf{A}}^{\xi}) \xi_b + \frac{1}{6} (\langle \underline{\mathbf{U}} \rangle_e \cdot \underline{\mathbf{A}}^{\eta}) \eta_b$$

$$B^e_{ab} \qquad \frac{\Delta t}{2} \int_{\Lambda^e} (\underline{\mathbf{U}} \cdot \underline{\nabla} N_a)(\underline{\mathbf{U}} \cdot \underline{\nabla} N_b) \, \mathrm{d}\Lambda^e = \frac{\Delta t}{8S_e} ((\langle \underline{\mathbf{U}} \rangle_e \cdot \underline{\mathbf{A}}^{\xi})(\langle \underline{\mathbf{U}} \rangle_e \cdot \underline{\mathbf{A}}^{\xi})(\xi_a \xi_b) + (\langle \underline{\mathbf{U}} \rangle_e \cdot \underline{\mathbf{A}}^{\eta})(\langle \underline{\mathbf{U}} \rangle_e \cdot \underline{\mathbf{A}}^{\eta})(\eta_a \eta_b) + (\langle \underline{\mathbf{U}} \rangle_e \cdot \underline{\mathbf{A}}^{\xi})(\langle \underline{\mathbf{U}} \rangle_e \cdot \underline{\mathbf{A}}^{\eta})(\xi_a \eta_b + \eta_a \xi_b))$$

APPENDIX B: NOMENCLATURE

$\underline{\mathbf{B}}$	BTD vector
B^e_{ab}	BTD matrix
C_D	Drag coefficient
C_L	Lift coefficient
C^e_{ab}	Convection matrix
D	A characteristic diameter
D^e_{ab}	Diffusion matrix
$D^e_{x,ab}$	$\partial/\partial x$ matrix
$D^e_{y,ab}$	$\partial/\partial y$ matrix
$\underline{\mathbf{F}}$	Body force vector
$\tilde{F}_D$	Drag force
$\tilde{F}_L$	Lift force
$\underline{\tilde{\mathbf{F}}}_S$	Surface force
f	Frequency of the vortex shedding
$\underline{\mathbf{f}}_{\mathrm{adv}}$	Convection vector
$\underline{\mathbf{i}}$	Unit base vector in x direction
$\underline{\mathbf{j}}$	Unit base vector in y direction
M^e_{ab}	Mass matrix
m^e	Number of elements
N_a	Shape or trial function of node a
$\underline{\mathbf{n}}$	Outward normal unit vector
$\underline{\mathbf{n}}_s$	Unit normal vector (directed into the bluff body)
P	Dimensionless pressure

Re	Reynolds number
St	Strouhal number
T_C	Convective time scale
T_D	Viscous time scale
t	Dimensionless time
$\underline{\mathbf{U}}$	Velocity vector
u_a	Velocity of node a in x-direction
U_b	A characteristic velocity
v_a	Velocity of node a in y-direction
x	X coordinate
y	Y coordinate

Greek letters

μ	Viscosity
ρ	Density
Λ^e	Domain of element
Γ	Boundary
$\underline{\nabla}$	Gradient operator
$\underline{\underline{\tau}}$	Viscous stress tensor

Superscript

k	kth time step
e	Element

Subscript

a	Nodal index
b	Nodal index
tr	Transpose operator

REFERENCES

1. Kovacs A, Kawahara M. A finite element scheme based on the velocity correction method for the solution of the time-dependent incompressible Navier–Stokes equation. *International Journal for Numerical Methods in Fluids* 1991; **13**:403–423.
2. Arnal MP, Goering DJ, Humphrey JAC. Vortex shedding a bluff body adjacent to a plane sliding wall. *Journal of Fluids Engineering* 1991; **113**:384–397.
3. Natarajan R. A numerical method for incompressible viscous flow simulation. *Journal of Computational Physics* 1992; **100**:384–395.
4. Red G, Utnes T. A Finite element solution of the time-dependent incompressible Navier–Stokes equations using a modified velocity correction method. *International Journal for Numerical Methods in Fluids* 1993; **17**: 346–364.
5. Suzuki H, Inoue Y, Nishimura T, Fukutani K, Suzuk K. Unsteady flow in a channel obstructed by a square rod (crisscross motion of vortex). *International Journal for Heat and Fluid Flow* 1993; **14**(1):2–9.
6. Li G, Humphrey JAC. Numerical modelling of confined flow past a cylinder of square cross-section at various orientations. *International Journal for Numerical Methods in Fluids* 1995; **20**:1215–1236.
7. Bentley JP, Benson RA, Shanks AJ. The development of dual body vortex flowmeters. *Flow Measurement Instrument* 1996; **7**(2):85–90.

8. Okajima A. Strouhal number of rectangular cylinders. *Journal of Fluid Mechanics* 1982; **123**:379–398.
9. Young JA. Viscous flow around vortex shedding flowmeters: A discrete vortex model. *PhD Thesis*, Department of Aeronautics, Imperial College, UK, 1989.
10. Davis RW, Moore EF. A numerical study of vortex shedding from rectangles. *Journal of Fluid Mechanics* 1982; **123**:379–398.
11. Vickery BJ. Fluctuating lift and drag on a long cylinder of square cross-section in a smooth and in a turbulent stream. *Journal of Fluid Mechanics* 1966; **25**:481–494.
12. Spitzer DW. *Flow Measurement.* Instrument Society of America, 1996.
13. Taylor C, Hughes TG. *Finite Element Programming of the Navier–Stokes Equations.* Pineridge Press: Swansea, UK, 1981.
14. Bird RB. *Transport Phenomena.* Wiley: Chichester, 1960.
15. Peyret R, Taylor TD. *Computational Methods for Fluid Flow.* Springer-Verlag: New York, 1990.
16. Jan YJ, Huang SJ, Lee TY. Computational fluid flow in two dimensions using simple T4/C3 element. *International Journal for Numerical Methods in Fluids* 2000; **34**:187–205.
17. Press WH, Teukolsky SA, Vetterling WT, Flannery BP. *Numerical Recipes in Fortran.* Cambridge, 2nd edition, 1992.
18. Silvester PP, Ferrari RL. *Finite Elements for Electrical Engineers.* Cambridge, 2nd edition, 1990:323–326.
19. Gresho PM, Chan ST, Lee RL, Upson CD. A modified finite element method for solving the time-dependent incompressible Navier–Stokes equations. Part 1: theory. *International Journal for Numerical Methods in Fluids* 1984; **4**:557–598.
20. Gresho PM, Chan ST, Lee RL, Upson CD. A modified finite element method for solving the time-dependent incompressible Navier–Stokes equations. Part 2: applications. *International Journal for Numerical Methods in Fluids* 1984; **4**:619–640.
21. Gresho PM. Incompressible fluid dynamics: some fundamental formulation issues. Annual Review. *Fluid Mechanics* 1991; **23**:413–453.
22. Blevins RD. *Flow-Induced Vibration.* Van Nostrand Reinhold Company, 1990.
23. Ghia U, Ghia KN, Shin CT. High-Re solution for incompressible flow using the Navier–Stokes equations and a multigrid method. *Journal of Computational Physics* 1982; **48**:387–411.
24. Donea J, Giuliani S, Laval H, Quartapelle L. Finite element solution of the unsteady Navier–Stokes equations by a fractional step method. *Computer Methods in Applied Mechanics Engineering* 1982; **30**:53–73.
25. Kim J, Moin P. Application of fractional-step method to incompressible Navier–Stokes equation. *Journal of Computational Physics* 1985; **59**:308–323.
26. Gresho PM. On the theory of semi-implicit projection methods for viscous incompressible flow and its implementation via a finite element method that also introduces a nearly consistent mass matrix. Part 1: theory. *International Journal for Numerical Methods in Fluids* 1990; **11**:587–620.
27. Lee BE. The effect of turbulence on the surface pressure field of a square prism. *Journal of Fluid Mechanics* 1975; **69**:263–282.
28. Davis RW, Moore EF, Purtell LP. A numerical experimental study of confined flow around rectangular cylinders. *Physics of Fluids* 1984; **27**:46–59.

